Spin Reorientation in Antiferromagnetic Layered FePt$_5$P

Xin Gui, Madalynn Marshall, Ranuri S. Dissanayaka Mudiyanselage, Ryan A. Klein, Qiang Chen, Qiang Zhang, William Shelton, Haidong Zhou, Craig M. Brown, Huibo Cao, Martha Greenblatt, and Weiwei Xie*

Read Online

ACCESS | Metrics & More | Article Recommendations | Supporting Information

ABSTRACT: FePt$_5$P, a substitutional variant of the anti-CeCoIn$_5$ structure type in the space group $P4/mmm$, was synthesized by a high-temperature solid-state method and structurally characterized by X-ray diffraction. FePt$_5$P contains layers of FePt$_{12}$ clusters formed by magnetically active Fe and heavy Pt with strong spin-orbit coupling (SOC); the layers are separated by P atoms. The various Fe−Pt distances in FePt$_{12}$ clusters generate complex magnetic orders in FePt$_5$P. According to temperature-dependent magnetic and specific heat measurements, FePt$_5$P shows a stripe-type antiferromagnetic order at $T_N \approx 90$ K, which is also confirmed by resistivity measurements. Moreover, a spin reorientation occurs at ∼74 and ∼68 K in and out of the ab plane based on the specific heat measurements. The temperature-dependent neutron powder diffraction patterns demonstrate the antiferromagnetic order in FePt$_5$P, and the spins orientate up to 58.4° with respect to the c axis at 10 K. First-principles calculations of FePt$_5$P show the band splitting at the Fermi level by strong SOC and the s−d hybridization between P and Fe/Pt electrons enhances the structural stability and affects the magnetic ordering.

KEYWORDS: *layered magnetism, spin-orbit coupling, neutron scattering, spin reorientation, antiferromagnetic spintronics*
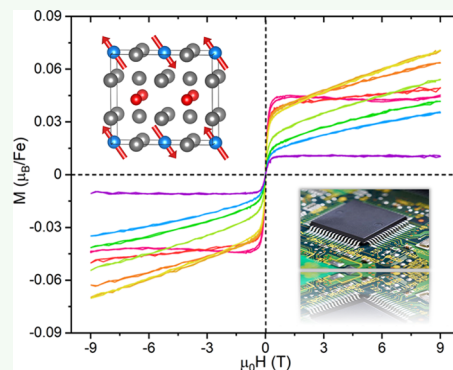
INTRODUCTION

Design and synthesis of magnetic materials with targeted tunable phenomena have been grand challenges in the materials community for decades. Applying structure−magnetism relationships for materials discovery is a widely used chemical rule. Intermetallic compounds with flexible stoichiometry and tunable valence electron counts are ideal platforms to study the structure-magnetism relationship and to predict the magnetic properties, for example, in the itinerant magnets Ti$_3$Co$_5$B$_2$-type[1−4] and AlCo$_2$B$_2$-type[5,6] structures.[7,8]

Recently, we discovered a new family of compounds with the MgPt$_5$As-type structure, such as the rare-earth-free ferromagnetic (FM) MnPt$_5$As, antiferromagnetic (AFM) MnPt$_5$P, and YbPt$_5$P.[9−11] These new compounds exhibit various magnetic behaviors ranging from ferromagnetism and antiferromagnetism due to complex atomic interactions between magnetically active elements (Mn and Yb) separated by non-magnetic stacking layers.

One approach by solid-state chemists to tune magnetic ordering in new phases is to adjust the valence electron counts. However, the magnetic states in materials can also be manipulated and detected by introducing elements with strong spin-orbit coupling (SOC) on non-magnetic sites. For example, non-magnetic noble metals with large SOC including Rh, Pt, and W have been shown to tune the spin orientation.[12] Moreover, SOC effects in magnetic materials are crucial for other spin-

transfer effects, such as spin penetration length,[13,14] giant magnetoresistance (GMR),[15] and enhanced spin pumping, which are critical to the spintronic devices in information technology.[16] When the SOC effect from Ir/Pt/Au is coupled with 3d electrons from Mn, the appearance of GMR and anisotropic magnetoresistance (AMR) is appreciable, as in MnX.[17−21] In addition, the thickness of the antiferromagnetic layers is a key factor to tune the magnitude of existing spin-transfer effects.[22−25]

Herein, a new bulk AFM material FePt$_5$P that couples a layered structure with strong SOC was discovered and synthesized. FePt$_5$P crystallizes with a layered structure, analogous to the well-known layered heavy-fermion super-conductor, CeCoIn$_5$.[26,27] With the high concentration of Pt per formula unit, it is expected that strong SOC effects are introduced by the Pt atoms. The FePt$_{12}$ polyhedral layers are separated by P layers in FePt$_5$P. Such polyhedral clusters are also found in AFM FePt$_3$ consisting of similar FePt$_{12}$ polyhedra.[28,29] Neutron powder diffraction measurements show a clear AFM
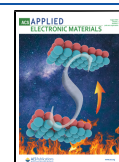
ordering transition at $T_N \approx 90$ K. Spin reorientations were observed at lower temperatures, ~68 and ~74 K along the c axis and in the ab plane, respectively. Large magnetoresistance at 9 T ($\Delta\rho/\rho_0 \sim 35\%$) at 1.7 K is found by field-dependent resistivity measurements, which is frequently observed in AFM spintronic candidates.[22] First-principles calculations indicate that the SOC and AFM ordering significantly affect the electronic structures near the Fermi energy in $FePt_5P$.

EXPERIMENTAL SECTION

Sample Preparation. $FePt_5P$ can be synthesized *via* a high-temperature solid-state method. The mixture of Fe powder (−200 mesh, 99 + %, Alfa Aesar), Pt powder (−22 mesh, 99.99%, BTC), and red P powder (−100 mesh, 99%, BTC) was thoroughly mixed with a molar ratio of 1:5:1.[a] The mixture was pressed into a solid pellet. The pellet was placed into an alumina crucible and then sealed into an evacuated silica tube (< 10^{-5} torr). The sealed tube was slowly heated up to 1050 °C at a rate of 30 °C per hour to prevent phosphorus from exploding. After annealing at 1050 °C for 2 days, the sample was slowly cooled down to room temperature in 10 days. Polycrystalline $FePt_5P$ is obtained by this process. Small single crystals (~$0.8 \times 0.8 \times 0.2$ mm³) are found to be detachable from the sample bulk. The material is stable in the ambient air and humidity.

Phase Identification. To determine the phase purity, the room-temperature powder X-ray diffraction (PXRD) pattern was collected on a Rigaku MiniFlex 600 powder X-ray diffractometer with Cu Kα radiation ($\lambda = 1.5406$ Å, Ge monochromator). The experiment was performed with the 2θ angle between 5 and 90° with a step of 0.005° at a rate of 0.1°/min. Rietveld fitting on the FullProf Suite was employed to obtain the weight percentage of obtained phases.[30] The temperature-dependent PXRD patterns were measured every 10 K from 300 to 10 K with a HUBER X-ray diffractometer equipped with a helium cryogenic. The LeBail refinement was performed on each pattern to obtain the phase information and accurate lattice parameters.[31,32]

Structure Determination. The crystal structure of $FePt_5P$ was determined using a Bruker Apex II single crystal X-ray diffractometer coupled with Mo radiation ($\lambda_{K\alpha} = 0.71073$ Å) at room temperature. To ensure the homogeneity, multiple pieces of crystals (~$15 \times 50 \times 50$ μm³) from different batches were measured. The crystals were mounted on a Kapton loop and protected by glycerol. Four different crystal and detector orientations were generated to take the measurement with an exposure time of 10 s per frame. The scanning 2θ width was set to 0.5°. Direct methods and full-matrix least-squares on F² models within the *SHELXTL* package were applied to solve the structure.[33] Data acquisition was performed *via* Bruker *SMART* software with the corrections on the Lorentz and polarization effect done by the *SAINT* program. Numerical absorption corrections were accomplished with *XPREP*.[33,34]

Neutron Powder Diffraction (NPD). Neutron powder diffraction patterns were collected on the time-of-flight (TOF) powder diffractometer (POWGEN) at the Spallation Neutron Source (SNS) at Oak Ridge National Laboratory (ORNL). The measurement was carried out at various temperatures of T = 10, 71, 80, 100, and 150 K using a neutron wavelength band of 0.97−2.033 Å with a central wavelength of 1.5 Å. A powder sample of ~3 g was loaded into a 6 mm diameter vanadium sample can with a copper gasket. The sample contains the $FePt_3$ impurity according to powder X-ray diffraction. The FullProf refinement suite and Sarah programs were used to solve the nuclear and magnetic structure.[30,32,35]

Scanning Electron Microscopy (SEM). The chemical compositions were confirmed using a high-vacuum scanning electron microscope (SEM) (JSM-6610 LV). Samples were placed on carbon tape prior to loading into the SEM chamber and were examined at 20 kV.

Physical Property Measurements. Magnetic properties, resistivity, and heat capacity measurements were performed on a Quantum Design Dynacool physical property measurement system (PPMS) with the temperature ranging from 1.8 to 300 K with and without applied fields of up to 9 T. The magnetic susceptibility is defined as $\chi = M/H$.

Here, M is the magnetization in units of emu, and H is the applied magnetic field. A standard relaxation calorimetry method was used to measure heat capacity, and the data were collected in a zero magnetic field between 1.8 and 220 K using N-type grease. All the measurements were performed on manually picked single crystal samples of $FePt_5P$.

Electronic Structure Calculations. The band structure and density of states (DOS) of $FePt_5P$ were calculated using the WIEN2k program, which has the full-potential linearized augmented plane wave method (FP-LAPW) with local orbitals implemented.[36] The electron exchange-correlation potential was used to treat the electron correlation within the generalized gradient approximation, which is parameterized in ref 37.[37] The conjugate gradient algorithm was applied, and the energy cutoff was set at 500 eV. Reciprocal space integrations were completed over an $8 \times 8 \times 4$ Monkhorst−Pack k-point mesh for non-magnetic calculation and $3 \times 12 \times 4$ for magnetic calculation.[38] With these settings, the calculated total energy converged to less than 0.1 meV per atom. The spin-orbit coupling (SOC) effects were only applied for Pt atoms. The structural lattice parameters obtained from single crystal X-ray diffraction (SC-XRD) are used for both calculations for non-magnetic calculation, while for magnetic calculation, the magnetic structure obtained from NPD was utilized.

RESULTS AND DISCUSSION

Crystal Structure and Phase Determination of $FePt_5P$. The crystal structure of $FePt_5P$ determined by single crystal XRD is shown in Figure 1a. The crystallographic data, including atomic coordinates, site occupancies, and equivalent isotropic thermal displacement parameters, are listed in Tables 1 and 2. As can be seen in Figure 1a, $FePt_5P$ adopts a layered tetragonal
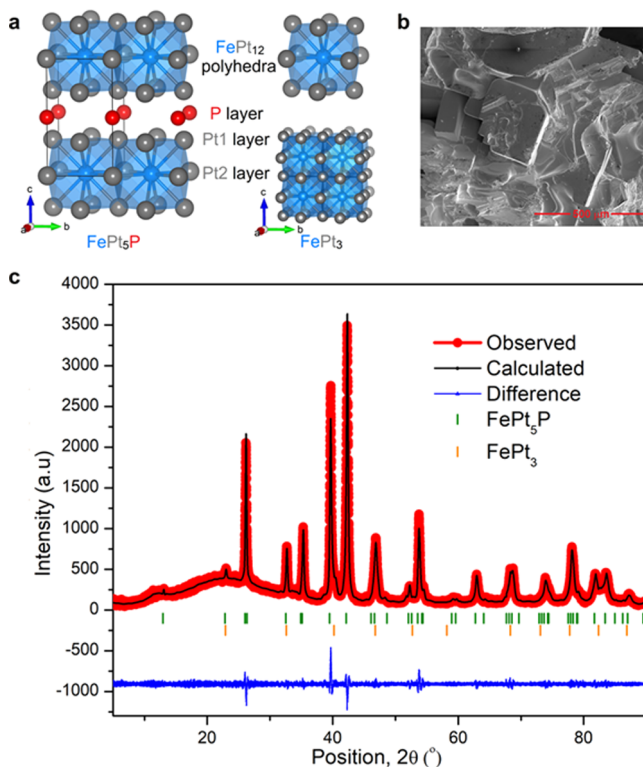

Figure 1. (a) Crystal structure of $FePt_5P$ and $FePt_3$. Blue, gray, and red balls represent Fe, Pt, and P atoms, respectively. (b) SEM picture of polycrystalline $FePt_5P$ with a layered feature. (c) Powder XRD pattern with Rietveld fitting of polycrystalline $FePt_5P$. The red line with ball indicates the observed pattern, the black line represents the calculated pattern of $FePt_5P$, and the blue line stands for the residual intensities. The Bragg peak positions of different phases are indicated by the vertical ticks.

**Table 1. Single Crystal Structure Refinement for FePt₅P at 296 (2) K**

refined formula	FePt₅P
F.W. (g/mol)	1062.27
space group; Z	P4/mmm; 1
a (Å)	3.901 (1)
c (Å)	6.857 (3)
V (Å³)	104.4 (1)
θ range (°)	2.971−30.321
no. reflections; R_{int}	484; 0.0262
no. independent reflectionsno. parameters	127
	12
R_1: ωR_2 $(I > 2\delta(I))$	0.0262; 0.0609
goodness of fit	1.125
diffraction peak and hole (e⁻/ Å³)	4.557; −1.849

[a]Values in parentheses indicate one standard deviation.

Table 2. Atomic Coordinates and Equivalent Isotropic Displacement Parameters for FePt₅P at 296 (2) K[a]

atom	Wyckoff	Occ.	x	y	z	U_{eq}
Pt1	4i	1	0	1/2	0.2884 (1)	0.0104 (3)
Pt2	1a	1	0	0	0	0.0103 (4)
Fe3	1c	1	1/2	1/2	0	0.011 (1)
P4	1b	1	0	0	1/2	0.012 (2)

[a]U_{eq} is defined as one-third of the trace of the orthogonalized U_{ij} tensor (Å²). Values in parentheses indicate one standard deviation.
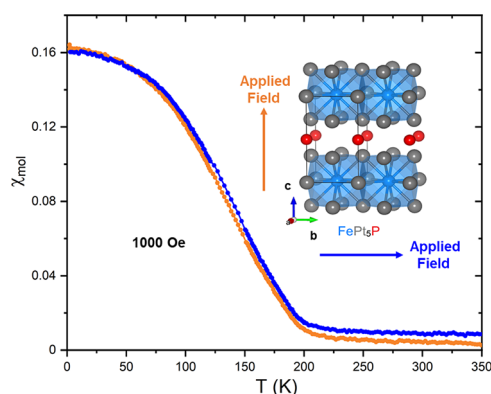
Figure 2. Temperature-dependence of magnetic susceptibility of FePt₅P crystals with the magnetic field applied (blue: parallel to the c axis; orange: perpendicular to the c axis) from 1.8 to 350 K.

structure with the space group P4/mmm. In FePt₅P, the face-sharing FePt₁₂ polyhedral cluster layers are separated by P layers. By comparing it with the crystal structure of binary FePt₃ also shown in Figure 1a, it is seen that similar FePt₁₂ polyhedra exist in FePt₃.[29,39] The Fe−Pt bond distances in FePt₅P within the ab plane and out of the ab plane are 2.757 (1) Å and 2.776 (1) Å respectively, both which are slightly longer than Fe−Pt bond lengths in FePt₃ (2.738 (1) Å). The significant difference between FePt₅P and FePt₃ is the Fe−Fe distance, which doubles in FePt₅P along the c axis and contributes to the magnetic anisotropy in FePt₅P. The SEM image of the FePt₅P chunk is shown in Figure 1b where the layered structural feature is easily observed.

The phase purity of polycrystalline FePt₅P was examined by PXRD at 300 K. The Rietveld refined powder pattern is shown in Figure 1c. FePt₃ was included in the refinement as the impurity. According to the results, the weight percentages of FePt₃ is 4.72
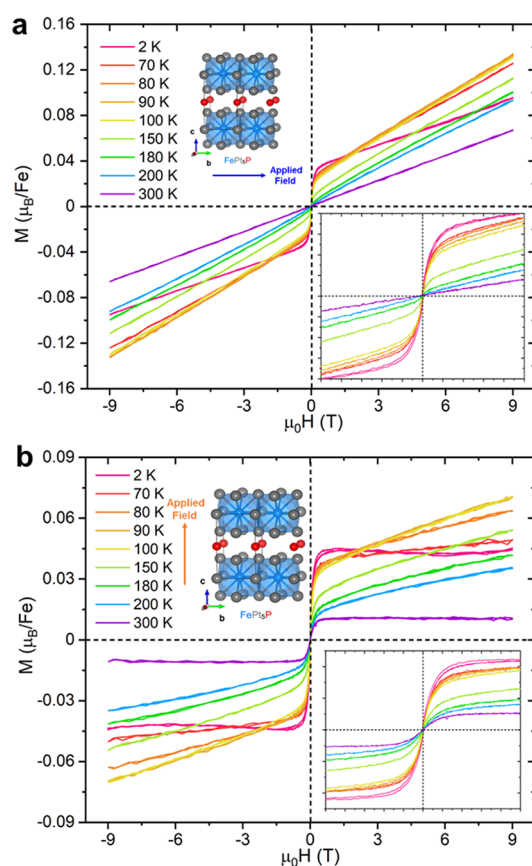
Figure 3. Hysteresis loops of FePt₅P at various temperatures with an external magnetic field from −9 to 9 T: (a) Perpendicular to the c axis and (b) parallel to the c axis. The inset of figures shows the enlarged figure at a low field range between −1 and 1 T.

(1) wt %. The refinement results R_p, R_{wp}, and χ^2 are 5.01, 6.53, and 1.05, respectively, which indicate a reasonable PXRD refinement.

Magnetic Properties of Single Crystal FePt₅P. Magnetic properties of FePt₅P were measured on the small single crystals with a small portion of FePt₃ impurity. The single crystals are sequentially aligned with two different orientations: the external magnetic field is first perpendicular (B⊥c) and then parallel to the c axis (B//c) in two separate measurements. The results of temperature dependence of magnetic susceptibility are presented in Figure 2 with an applied magnetic field of 1000 Oe. The magnetic susceptibility shows an upturn starting from 200 K, which originates from the impurity FePt₃, and as the temperature decreases, the magnetic susceptibility increases and reaches a plateau below ∼90 K. Similar magnetic behaviors are seen by both zero-field cooling (ZFC) and field cooling (FC) in Figure S1. When the applied magnetic field was parallel to the c axis, the magnitude of magnetic susceptibility is nearly identical but with a slightly smaller value in the high temperature region (>200 K), which implies a small magnetic anisotropy. With increasing the applied magnetic fields (Figure S1), the transitions occurring between 65 and 90 K appear, which is consistent with our neutron scattering measurements described below. The hysteresis loop of FePt₅P is shown in Figure 3. The results from both applied magnetic field directions imply soft magnetic behavior. Weak magnetic anisotropy is observed. Interestingly, when the applied magnetic field is parallel to the c axis, the magnetization of the sample shows a small, saturated
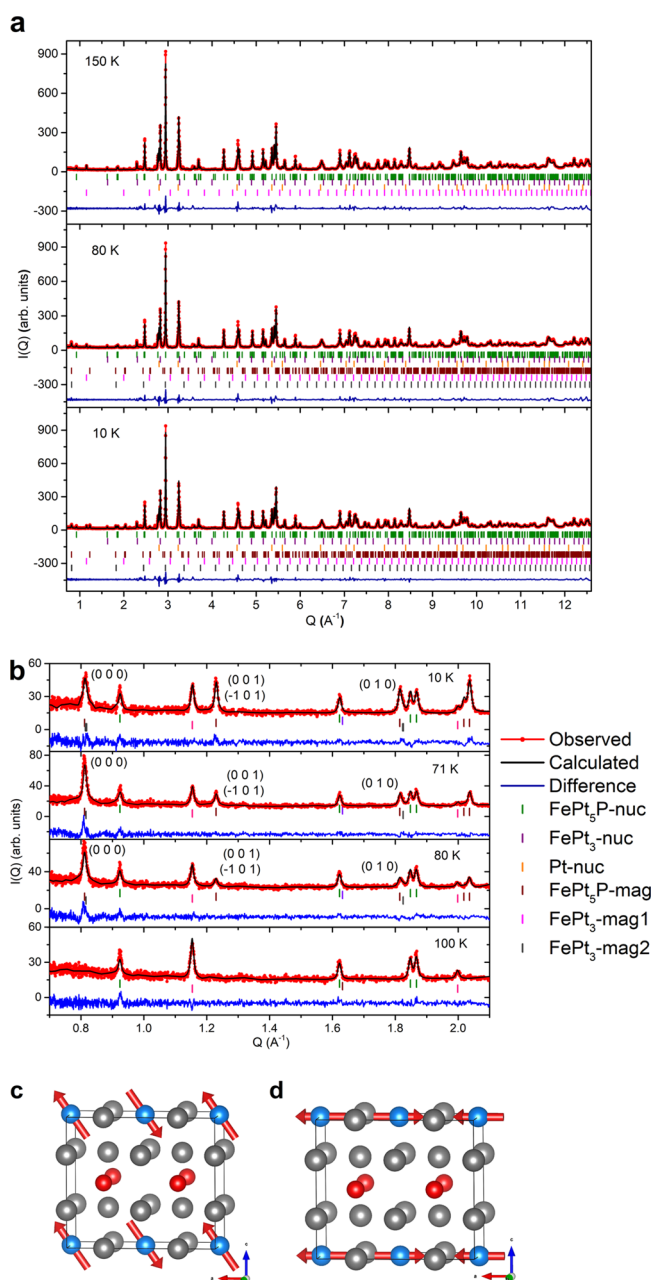
Figure 4. (a) Refined neutron powder diffraction patterns at 150, 80, and 10 K. (b) Enlarged low-Q region for refined patterns at 10, 71, 80, and 100 K. The lattice plane marked on the figure indicates where the magnetic peaks originate. (c) Magnetic structure of FePt$_5$P refined from NPD. (d) Hypothetical magnetic structure without spin reorientation for theoretical calculations.
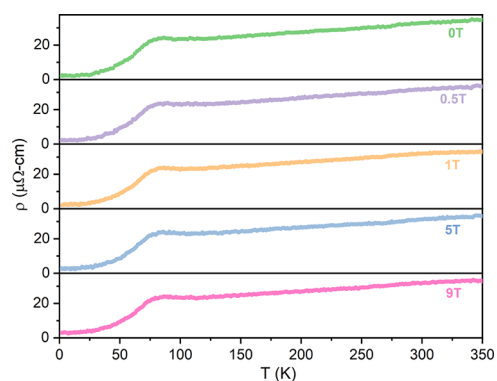

Figure 5. Temperature dependence of resistivity measured between 1.7 and 350 K under different external magnetic fields (0, 0.5, 1, 5, and 9 T).
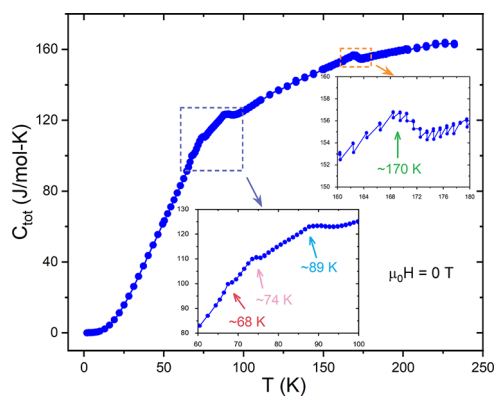

Figure 6. Heat capacity of the FePt$_5$P crystal between 1.8 and 225 K without an applied magnetic field. The insets show the enlarged picture of entropy change regions.

moment of ~0.010 μ_B/Fe in Figure 3b after subtracting the FePt$_3$'s magnetic contribution. However, the hysteresis loop of FePt$_5$P with the applied magnetic field parallel to the c axis shows a linear increase till ~0.06 μ_B/Fe at 9 T and 300 K, which still does not reach saturation. Moreover, when the sample was cooled down, both orientations displayed larger absolute values of the slope down to 90 K where the magnetizations at 9 T reached their maxima. After the temperature was decreasing to below 90 K, i.e., 80 K, the absolute value of the slope dropped along with the decrease of the magnetization value. This indicated that another magnetic ordering of FePt$_5$P occurred near 90 K.

Magnetic Structure of FePt$_5$P. Time-of-flight (TOF) neutron powder diffraction (NPD) data was collected at POWGEN (Oak Ridge National Laboratory) to determine the magnetic structures of FePt$_5$P at various temperatures. Figure 4a shows the refined neutron diffraction patterns measured at 150, 80, and 10 K. Two impurity phases are identified in the sample including FePt$_3$ and Pt, which is consistent with PXRD results. The crystal structures of FePt$_5$P, FePt$_3$ and Pt reproduce well the peaks observed at 180 and 300 K, as shown in Figure S2. The analysis of NPD data further confirms the tetragonal $P4/mmm$ structure of FePt$_5$P, in agreement with the PXRD results. Above 150 K, the magnetic reflections can be indexed with a propagation vector $k = (1/2, 1/2, 0)$, belonging to the FePt$_3$ phase.[28,40] The minor peaks, which cannot be included in the FePt$_5$P or FePt$_3$ phases, are also examined and compared at all the temperatures. It can be concluded that these minor peaks present are not temperature-dependent and have no contribution to the magnetic phases of FePt$_5$P. Further cooling down to 80 K, additional magnetic reflections are observed associated with the AFM order in FePt$_5$P, as shown in Figure 4b. These magnetic reflections can be indexed with the propagation vector $k = (1/2, 0, 0)$. The magnetic peaks from typical lattice planes of FePt$_5$P $((0\ 0\ 0), (0\ 0\ 1), (-1\ 0\ 1), (0\ 1\ 0))$ were gradually suppressed when the temperature was increased up to 100 K. The refinement using the unit cell $2a \times b \times c$ revealed FePt$_5$P to have a stripe-type AFM ordering with the magnetic space group $P_a mma$ (#51.298) including FM bc planes coupling AFM along the a axis. NPD measurements performed at 70 K consist of similar magnetic
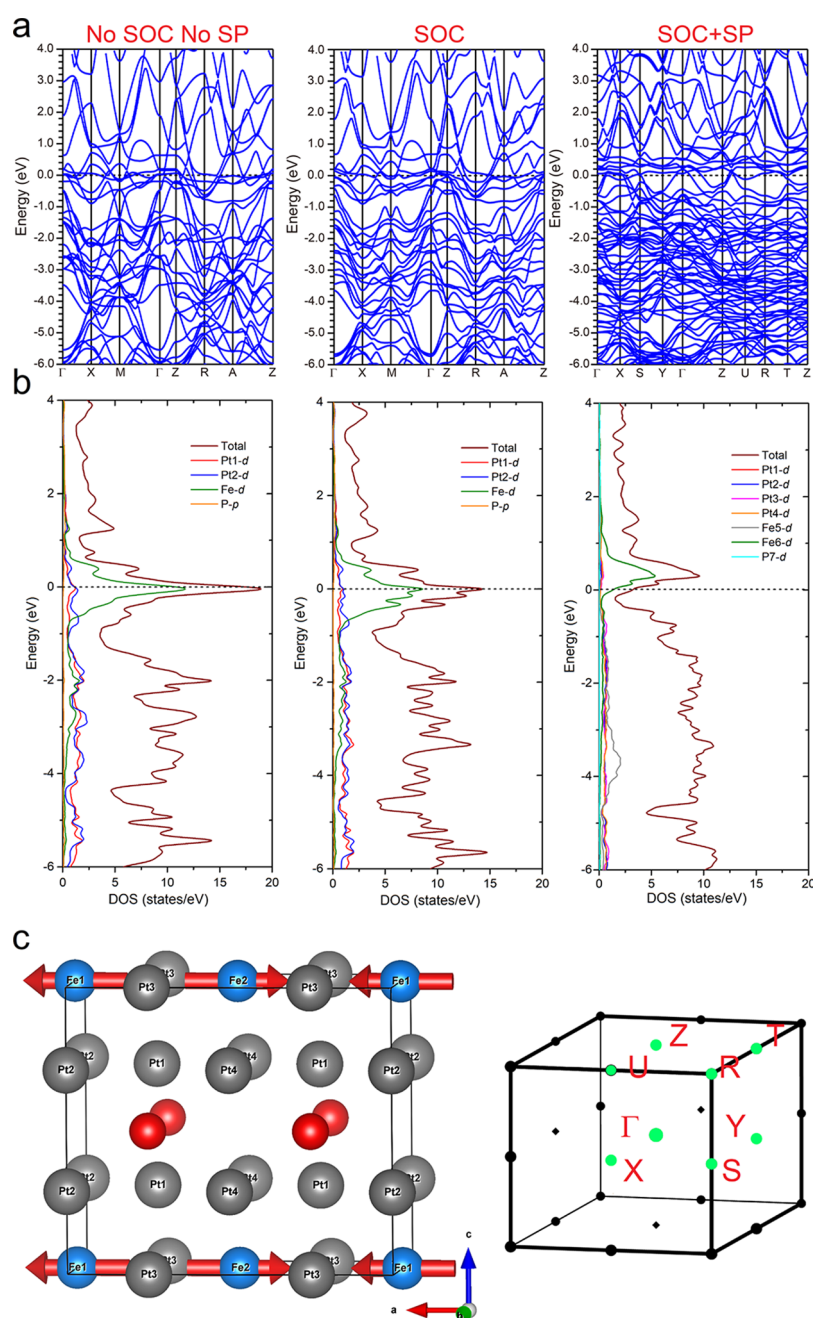
Figure 7. (a) Band structures of FePt$_5$P with/without consideration of the SOC effect and SP. (b) Density of states of FePt$_5$P corresponding to panel a. (c) Magnetic unit cell and Brillouin zone of magnetically ordered FePt$_5$P.

reflections as those at 80 K. Thus, the ordered moments are 2.2 (2) μ_B/Fe and 2.8 (1) μ_B/Fe at 80 and 70 K, respectively. A second magnetic transition of FePt$_3$ also occurred at 80 K and was indexed using the k vector (0, 0, 1/2).[29] The magnetic structure of FePt$_3$ has a stripe-type AFM ordering along the a axis with an ordered moment of 1.01 (3) μ_B/Fe at 80 K. The NPD data collected at 10 K reveals no new reflections; however, a rotated AFM axis for FePt$_5$P is observed. The resulting ordered moment for this state was determined to have the components m_a = 3.0 (2) μ_B/Fe and m_c = 1.8 (3) μ_B/Fe with a total ordered moment of m_{tot} = 3.5 (3) μ_B/Fe. Considering the ordered moments along the a and c directions, the rotated angle of the AFM axis was calculated to deflect toward the c axis and determined to be ~58.4°. The magnetic structures for FePt$_5$P, with and without spin reorientations, are shown in Figure 4c,d.

Resistivity and Heat Capacity of FePt$_5$P Crystals. A four-probe method was applied to measure the resistivity on one of the larger pieces of crystals used in magnetic property measurements. The temperature dependence of resistivity under five different magnetic fields, 0, 0.5, 1, 5, and 9 T, is presented in Figure 5a. The resistivity of FePt$_5$P showed similar linear $\rho(T)$ behavior above ~118 K in all cases, as fitted by the white line, except the one measured under 1 T where a kink was observed around 300 K in Figure S4. The resistivity started to increase when the temperature dropped below ~118 K and reached a maximum at ~86 K. Based on the NPD results, that the magnetic ordering of FePt$_5$P starts between 80 and 100 K, the increasing $\rho(T)$ at ~118 K could be due to the small amount of ordered FePt$_3$ impurity scattering the electrons of FePt$_5$P. Moreover, the subsequent drop of resistivity can be interpreted

as the s−d electron scattering based on its T^3 behavior when fitted to $\rho(T) = \rho_0 + AT^n$ where ρ_0 is the residual resistivity due to defect scattering, A is a constant, and n is an integer determined by the interaction pattern. The magnetoresistance of FePt$_5$P displayed in Figure S3 implies that ∼35% magneto-resistance can be observed at 1.7 K at an applied magnetic field of 9 T. With increasing temperature, the large magnetoresistance was suppressed gradually (Figure S4).

Heat capacity measurement made on the same piece of crystal used in the resistivity measurement was performed without an applied magnetic field, and the result is presented in Figure 6. Four peaks are observed within the explored temperature range (1.8 to 225 K) at around 170, 89, 74, and 68 K. Based on previous results, the smaller peak around 170 K ($\Delta C \approx 3.5$ J mol^{-1} K^{-1}) can be attributed to the magnetic ordering of FePt$_3$ impurity, which is consistent with the suggested reason of resistivity increasing after 118 K. The heat capacity jumps of the other three peaks are ∼7.0 J mol^{-1} K^{-1} (∼89 K), ∼3.0 J mol^{-1} K^{-1} (∼74 K), and ∼4.2 J mol^{-1} K^{-1} (∼68 K). According to the NPD results, the three peaks at 89, 74, and 68 K reflect the entropy changes of the AFM transitions and spin reorientations along different directions of FePt$_5$P. The specific heat peak at 170 K is consistent with the magnetic reflections observed in the NPD at 150 K, which stem from the AFM transition of FePt$_3$.[29,39]

Electronic Structure of FePt$_5$P. The band structures calculated for FePt$_5$P are shown in Figure 7a. The projection of significant orbitals for each atomic site is also given in Figure S4. Spin-orbit coupling (SOC) effects from Pt and spin polarization (SP) from Fe were taken into account, and the comparison among band structures with/without those effects was also calculated. In the left two figures of Figure 7a, the band structures with/without consideration of the SOC effect are given, where the Brillouin zone (BZ) was generated from the original unit cell. Some of the bands around the Fermi level are split and lead to band gaps, such as the bands from ∼ −0.05 to ∼0.1 eV between Γ and X points. New saddle points are observed near the E_F when SOC is included, such as at the M point (Figure 7a). When including both SOC and SP, with the type of atoms and construction of the BZ shown in Figure 7c, the density of bands near E_F is less compared with the one where only the SOC effect is considered. Fewer saddle points can also be seen at the Fermi level (with SOC and SP), which indicates a more stable state for FePt$_5$P. The contribution of both SOC and SP to stability of FePt$_5$P is recognized intuitively in Figure 7b, which lists the density of states (DOS) corresponding to band structures in Figure 7a. It is clear in Figure 7b that the DOS at E_F decreases dramatically with SOC and SP included. Moreover, the E_F in the SOC + SP case is moving toward a pseudo gap at ∼ −0.2 eV. The Fe-d orbitals have the largest contribution at the Fermi energy, far larger than that of Pt and P atoms, which is also displayed in Figure S5.

CONCLUSIONS

In this paper, we synthesized the first ternary compound in the Fe−Pt−P system, FePt$_5$P, which crystallizes in a layered tetragonal structure in the space group $P4/mmm$ and orders antiferromagnetically along the c direction of the unit cell below $T_N \approx 90$ K. The spins are reoriented below ∼68 K. Resistivity measurements indicate metallic behavior and the dominance of s−d scattering below T_N. First-principles calculations of electronic structure show s−d electronic interaction governing the resistivity in FePt$_5$P, which is heavily influenced by the effect of SOC and magnetism. The new material serves as an ideal model for the investigation of the relationship of magnetism, structure, and spin-orbit coupling in low-dimensional correlated electronic phases with constituent atoms of coupled magnetic and spin-orbit couple properties, respectively.

■ ASSOCIATED CONTENT

ⓈI Supporting Information

The Supporting Information is available free of charge at https://pubs.acs.org/doi/10.1021/acsaelm.1c00459.

CIF file of FePt$_5$P (CIF)

Magnetic susceptibility of FePt$_5$P; Magnetic structure of FePt$_3$ at 150 K; Magnetoresistivity at various temperatures; Projection of orbitals from Fe, Pt, and P atoms on band structure; Table of Rietveld refinement reliability factors; Low-temperature PXRD; Lattice parameters and volume of FePt$_5$P unit cell changes (PDF)

■ AUTHOR INFORMATION

Corresponding Author

Weiwei Xie − *Department of Chemistry and Chemical Biology, Rutgers University − New Brunswick, Piscataway, New Jersey 08854, United States;* ⓞ orcid.org/0000-0002-5500-8195; Email: weiwei.xie@rutgers.edu

Authors

Xin Gui − *Department of Chemistry, Princeton University, Princeton, New Jersey 08544, United States;* ⓞ orcid.org/0000-0003-0616-2150

Madalynn Marshall − *Department of Chemistry and Chemical Biology, Rutgers University − New Brunswick, Piscataway, New Jersey 08854, United States; Neutron Scattering Division, Oak Ridge National Laboratory, Oak Ridge, Tennessee 37831, United States*

Ranuri S. Dissanayaka Mudiyanselage − *Department of Chemistry and Chemical Biology, Rutgers University − New Brunswick, Piscataway, New Jersey 08854, United States*

Ryan A. Klein − *NIST Center for Neutron Research, National Institute of Standards and Technology, Gaithersburg, Maryland 20899, United States; Materials, Chemical, and Computational Sciences Directorate, National Renewable Energy Laboratory, Golden, Colorado 80401, United States*

Qiang Chen − *Department of Physics, University of Tennessee, Knoxville, Tennessee 37996, United States*

Qiang Zhang − *Neutron Scattering Division, Oak Ridge National Laboratory, Oak Ridge, Tennessee 37831, United States*

William Shelton − *Cain Department of Chemical Engineering, Louisiana State University, Baton Rouge, Los Angeles 70803, United States*

Haidong Zhou − *Department of Physics, University of Tennessee, Knoxville, Tennessee 37996, United States*

Craig M. Brown − *NIST Center for Neutron Research, National Institute of Standards and Technology, Gaithersburg, Maryland 20899, United States;* ⓞ orcid.org/0000-0002-9637-9355

Huibo Cao − *Neutron Scattering Division, Oak Ridge National Laboratory, Oak Ridge, Tennessee 37831, United States*

Martha Greenblatt − *Department of Chemistry and Chemical Biology, Rutgers University − New Brunswick, Piscataway, New Jersey 08854, United States;* ⓞ orcid.org/0000-0002-1806-2766

■ ADDITIONAL NOTE

[a]Certain commercial equipment, instruments, or materials (or suppliers, or software, etc.) are identified in this paper to foster understanding. Such identification does not imply recommendation or endorsement by the National Institute of Standards and Technology nor does it imply that the materials or equipment identified are necessarily the best available for the purpose.

■ REFERENCES

(1) Burghaus, J.; Dronskowski, R.; Miller, G. J. Slater−Pauling Behavior within Quaternary Intermetallic Borides of the $Ti_3Co_5B_2$ Structure-Type. *J. Solid State Chem.* **2009**, *182*, 2613−2619.

(2) Shankhari, P.; Scheifers, J. P.; Hermus, M.; Yubuta, K.; Fokwa, B. P. T. Unexpected Trend Deviation in Isoelectronic Transition Metal Borides $A_3T_5B_2$ (A = Group 4, T = Group 9): $Ti_3Co_5B_2$- vs. Perovskite-Type Studied by Experiments and DFT Calculations. *Z. Anorg. Allg. Chem.* **2017**, *643*, 1551−1556.

(3) Shankhari, P.; Zhang, Y.; Stekovic, D.; Itkis, M. E.; Fokwa, B. P. T. Unexpected Competition between Antiferromagnetic and Ferromagnetic States in $Hf_2MnRu_5B_2$: Predicted and Realized. *Inorg. Chem.* **2017**, *56*, 12674−12677.

(4) Zhang, Y.; Miller, G. J.; Fokwa, B. P. T. Computational Design of Rare-Earth-Free Magnets with the $Ti_3Co_5B_2$-Type Structure. *Chem. Mater.* **2017**, *29*, 2535−2541.

(5) Chai, P.; Stoian, S. A.; Tan, X.; Dube, P. A.; Shatruk, M. Investigation of Magnetic Properties and Electronic Structure of Layered-Structure Borides AlT_2B_2 (T=Fe, Mn, Cr) and $AlFe_{2−x}Mn_xB_2$. *J. Solid State Chem.* **2015**, *224*, 52−61.

(6) Tan, X.; Chai, P.; Thompson, C. M.; Shatruk, M. Magnetocaloric Effect in $AlFe_2B_2$: Toward Magnetic Refrigerants from Earth-Abundant Elements. *J. Am. Chem. Soc.* **2013**, *135*, 9553−9557.

(7) Kovnir, K.; Reiff, W. M.; Menushenkov, A. P.; Yaroslavtsev, A. A.; Chernikov, R. V.; Shatruk, M. "Chemical Metamagnetism:" From Antiferromagnetic $PrCo_2P_2$ to Ferromagnetic $Pr_{0.8}Eu_{0.2}Co_2P_2$ via Chemical Compression. *Chem. Mater.* **2011**, *23*, 3021−3024.

(8) Kovnir, K.; Thompson, C. M.; Zhou, H. D.; Wiebe, C. R.; Shatruk, M. Tuning Ferro- and Metamagnetic Transitions in Rare-Earth Cobalt Phosphides $La_{1−x}Pr_xCo_2P_2$. *Chem. Mater.* **2010**, *22*, 1704−1713.

(9) Gui, X.; Xie, W. Crystal Structure, Magnetism, and Electronic Properties of a Rare-Earth-Free Ferromagnet: $MnPt_5As$. *Chem. Mater.* **2020**, *32*, 3922−3929.

(10) Gui, X.; Chang, T.-R.; Wei, K.; Daum, M. J.; Graf, D. E.; Baumbach, R. E.; Mourigal, M.; Xie, W. A Novel Magnetic Material by

(11) Gui, X.; Klein, R. A.; Brown, C. M.; Xie, W. Chemical Bonding Governs Complex Magnetism in $MnPt_5P$. *Inorg. Chem.* **2021**, *60*, 87−96.

(12) Gambardella, P.; Miron, I. M. Current-induced spin−orbit torques. *Philos. Trans. R. Soc., A* **2011**, *369*, 3175−3197.

(13) Acharyya, R.; Nguyen, H. Y. T.; Pratt, W. P.; Bass, J. A Study of Spin−Flipping in Sputtered IrMn Using Py-Based Exchange-Biased Spin-Valves. *J. Appl. Phys.* **2011**, *109*, No. 07C503.

(14) Merodio, P.; Ghosh, A.; Lemonias, C.; Gautier, E.; Ebels, U.; Chshiev, M.; Béa, H.; Baltz, V.; Bailey, W. E. Penetration Depth and Absorption Mechanisms of Spin Currents in $Ir_{20}Mn_{80}$ and $Fe_{50}Mn_{50}$ Polycrystalline Films by Ferromagnetic Resonance and Spin Pumping. *Appl. Phys. Lett.* **2014**, *104*, No. 032406.

(15) Wang, Y.; Song, C.; Wang, G.; Miao, J.; Zeng, F.; Pan, F. Anti-Ferromagnet Controlled Tunneling Magnetoresistance. *Adv. Funct. Mater.* **2014**, *24*, 6806−6810.

(16) Frangou, L.; Oyarzún, S.; Auffret, S.; Vila, L.; Gambarelli, S.; Baltz, V. Enhanced Spin Pumping Efficiency in Antiferromagnetic IrMn Thin Films around the Magnetic Phase Transition. *Phys. Rev. Lett.* **2016**, *116*, No. 077203.

(17) Shick, A. B.; Khmelevskyi, S.; Mryasov, O. N.; Wunderlich, J.; Jungwirth, T. Spin-Orbit Coupling Induced Anisotropy Effects in Bimetallic Antiferromagnets: A Route towards Antiferromagnetic Spintronics. *Phys. Rev. B* **2010**, *81*, 212409.

(18) Park, B. G.; Wunderlich, J.; Martí, X.; Holý, V.; Kurosaki, Y.; Yamada, M.; Yamamoto, H.; Nishide, A.; Hayakawa, J.; Takahashi, H.; Shick, A. B.; Jungwirth, T. A Spin-Valve-like Magnetoresistance of an Antiferromagnet-Based Tunnel Junction. *Nat. Mater.* **2011**, *10*, 347−351.

(19) Wang, Y. Y.; Song, C.; Cui, B.; Wang, G. Y.; Zeng, F.; Pan, F. Room-Temperature Perpendicular Exchange Coupling and Tunneling Anisotropic Magnetoresistance in an Antiferromagnet-Based Tunnel Junction. *Phys. Rev. Lett.* **2012**, *109*, 137201.

(20) Galceran, R.; Fina, I.; Cisneros-Fernández, J.; Bozzo, B.; Frontera, C.; López-Mir, L.; Deniz, H.; Park, K.-W.; Park, B.-G.; Balcells, L.; Martí, X.; Jungwirth, T.; Martínez, B. Isothermal Anisotropic Magnetoresistance in Antiferromagnetic Metallic IrMn. *Sci. Rep.* **2016**, *6*, 35471.

(21) Wu, S. M.; Zhang, W.; KC, A.; Borisov, P.; Pearson, J. E.; Jiang, J. S.; Lederman, D.; Hoffmann, A.; Bhattacharya, A. Antiferromagnetic Spin Seebeck Effect. *Phys. Rev. Lett.* **2016**, *116*, No. 097204.

(22) Zhang, W.; Jungfleisch, M. B.; Jiang, W.; Pearson, J. E.; Hoffmann, A.; Freimuth, F.; Mokrousov, Y. Spin Hall Effects in Metallic Antiferromagnets. *Phys. Rev. Lett.* **2014**, *113*, 196602.

(23) Molina-Ruiz, M.; Lopeandía, A. F.; Pi, F.; Givord, D.; Bourgeois, O.; Rodríguez-Viejo, J. Evidence of Finite-Size Effect on the Néel Temperature in Ultrathin Layers of CoO Nanograins. *Phys. Rev. B* **2011**, *83*, 140407.

(24) Vallejo-Fernandez, G.; Fernandez-Outon, L. E.; O'Grady, K. Antiferromagnetic Grain Volume Effects in Metallic Polycrystalline Exchange Bias Systems. *J. Phys. D: Appl. Phys.* **2008**, *41*, 112001.

(25) Saglam, H.; Zhang, W.; Jungfleisch, M. B.; Sklenar, J.; Pearson, J. E.; Ketterson, J. B.; Hoffmann, A. Spin Transport through the Metallic Antiferromagnet FeMn. *Phys. Rev. B* **2016**, *94*, 140412.

(26) Movshovich, R.; Jaime, M.; Thompson, J. D.; Petrovic, C.; Fisk, Z.; Pagliuso, P. G.; Sarrao, J. L. Unconventional Superconductivity in $CeIrIn_5$ and $CeCoIn_5$: Specific Heat and Thermal Conductivity Studies. *Phys. Rev. Lett.* **2001**, *86*, 5152−5155.

(27) Izawa, K.; Yamaguchi, H.; Matsuda, Y.; Shishido, H.; Settai, R.; Onuki, Y. Angular Position of Nodes in the Superconducting Gap of Quasi-2D Heavy-Fermion Superconductor $CeCoIn_5$. *Phys. Rev. Lett.* **2001**, *87*, No. 057002.

(28) Bacon, G. E.; Crangle, J.; Sucksmith, W. Chemical and Magnetic Order in Platinum-Rich Pt + Fe Alloys. *Proc. R. Soc. London, Ser. A* **1963**, *272*, 387−405.

(29) Kohgi, M.; Ishikawa, Y. Magnetic Excitations in a Metallic Antiferromagnet $FePt_3$. *J. Phys. Soc. Jpn.* **1980**, *49*, 985−993.

Design: Observation of Yb^{3+} with Spin-1/2 in Yb_xPt_5P. *ACS Cent. Sci.* **2020**, *6*, 2023−2030.

(30) Rodríguez-Carvajal, J. Recent Advances in Magnetic Structure Determination by Neutron Powder Diffraction. *Phys. B: Condens. Matter* **1993**, *192*, 55−69.

(31) Le Bail, A.; Duroy, H.; Fourquet, J. L. Ab-Initio Structure Determination of $LiSbWO_6$ by X-Ray Powder Diffraction. *Mater. Res. Bull.* **1988**, *23*, 447−452.

(32) Dinnebier, R. E.; Billinge, S. J. L. Principles of Powder Diffraction. *Powder Diffraction: Theory and Practice*; The Royal Society of Chemistry's:, 2008. 1−19, DOI: 10.1039/9781847558237.

(33) Sheldrick, G. M. Crystal Structure Refinement with SHELXL. *Acta Crystallogr.* **2015**, *71*, 3−8.

(34) Bruker, S. *Bruker SMART (Version 5.625)*; Bruker AXS Inc.: Madison, Wisconsin, USA 2001.

(35) Wills, A. S. A New Protocol for the Determination of Magnetic Structures Using Simulated Annealing and Representational Analysis (SARA*h*). *Phys. B: Condens. Matter* **2000**, *276−278*, 680−681.

(36) Blöchl, P. E. Projector Augmented-Wave Method. *Phys. Rev. B* **1994**, *50*, 17953.

(37) Perdew, J. P.; Wang, Y. Accurate and Simple Analytic Representation of the Electron-Gas Correlation Energy. *Phys. Rev. B* **1992**, *45*, 13244−13249.

(38) King-Smith, R. D.; Vanderbilt, D. Theory of Polarization of Crystalline Solids. *Phys. Rev. B* **1993**, *47*, 1651−1654.

(39) Maat, S.; Hellwig, O.; Zeltzer, G.; Fullerton, E. E.; Mankey, G. J.; Crow, M. L.; Robertson, J. L. Antiferromagnetic Structure of **FePt₃** Films Studied by Neutron Scattering. *Phys. Rev. B* **2001**, *63*, 134426.

(40) Palaith, D.; Kimball, C. W.; Preston, R. S.; Crangle, J. Magnetic Behavior of the Pt+Fe System Near **Pt₃**Fe. *Phys. Rev.* **1969**, *178*, 795−799.